A Trihedral Corner Reflector for Radar Altimeter Calibration

Ferran Gibert^{ID}, Adrià Gómez-Olivé, Albert Garcia-Mondéjar^{ID}, Richard Francis^{ID}, Sergi Hernández^{ID}, Adrián Flores de la Cruz, Ester Vendrell, and Mònica Roca i Aparici

Abstract— A trihedral corner reflector has been used to evaluate the capability of passive reflectors to calibrate radar altimeters, such as the Poseidon-4 altimeter on board Sentinel-6A. The reflector location, placed on the top of a mountain ridge and about 4-km off-nadir of the Sentinel-6A subsatellite track, allows capturing echoed signals with a signal-to-clutter ratio (SCR) around 40 dB when processing the received data with a fully-focused synthetic aperture radar (FF-SAR) algorithm. Results obtained show a range bias of 33.9 with 8.5 mm of standard deviation and datation bias of −2.3 μs with a standard deviation of 1.8 μs for the measurement campaign between September 2021 and April 2022. Such values are comparable to what is currently achieved by means of active transponders, and therefore, it is demonstrated that passive reflectors may be of interest to support radar altimeter regular calibration.

Index Terms— Altimetry, calibration, corner reflector, fully focused synthetic aperture radar (FF-SAR), radar altimeter, Sentinel-6.

I. INTRODUCTION

DURING the last 30 years spaceborne radar altimeters have become fundamental instruments for ocean and general hydrosphere monitoring [1], [2]. In particular, radar altimeters have turned out to be key sensors for monitoring essential climate variables, such as the Global Mean Sea Level [3]. All spaceborne radar altimeters so far have required external calibration of their range measurements, which for pulsewidth limited instruments has been conventionally carried out over natural targets such as the ocean surface. The longest running such series, continuing since 1989, is from the Harvest platform [4]. Active transponders had also been developed and used (though relatively infrequently) for pulsewidth limited altimeters (e.g., [5]). These transponders have a receiving antenna directly coupled to a transmitting antenna via an amplification stage. Their internal delay is very short and they rely on the significant signal amplification to overcome clutter noise. We note that one different type of active transponder has been built, which retransmits a replica of the received signal after a delay corresponding to a path length of several kilometers to eliminate clutter. This is intended to calibrate the received echo power [6].

With the advent of altimeters which can operate in synthetic aperture radar (SAR) mode, starting with the CryoSat-2 mission in 2010 [7] and continuing with Sentinel-3 [8] and Sentinel-6 [9], these active transponders have become far more useful. Dedicated processing of the point target response, which is the transponder echo, essentially provides measurements of absolute range and associated time-stamping and also measurements of the instrument resolution in both range and azimuthal dimensions. Such transponders have been installed in Svalbard [10] (which is one of the original 1988 models, refurbished) and Crete [11].

The usage of passive reflectors instead of active transponders for radar altimeter range calibration was impractical for pulsewidth limited altimeters [now referred to as low-resolution mode (LRM)] due to the size required in order to achieve high enough signal-to-clutter ratio (SCR) for the reflected signal to be distinguished from the background clutter [12]. This is a direct function of the area of the instantaneously illuminated footprint. Although unfocused SAR (UF-SAR) processing, also called simple SAR mode [13], reduces this area, it is still uncomfortably large. Considering a requested SCR of at least 6 dB—considered a minimum for range calibration [14]—and assuming a low clutter scenario with backscatter coefficient not higher than 6 dB, the typical size of a triangular trihedral corner should already be larger than 7 m for LRM processed data or larger than 4 m if processed with a UF-SAR algorithm [14]. The resolution cells of both LRM and UF-SAR algorithms integrate all clutter from areas with along-track steps of 8–10 km or ∼300 m, respectively, and therefore, the reflector signal is mixed with the clutter from considerably large areas.

However, recent developments in radar altimetry processing techniques, such as fully focused SAR (FF-SAR) [15], allow to strongly improve the along-track resolution down to the ∼1-m scale, thus significantly reducing the size of the area contributing to clutter. Such improvement is of key importance for passive reflectors since it notably reduces the requested reflector side length to less than 2 m in order to get acceptable SCR, making them feasible in terms of practical application. It must be noted that the footprint side in UF-SAR and FF-SAR does not reduce in the cross-track direction but remains the same as in the LRM case.

Taking advantage of such an opportunity, a square-side trihedral corner reflector designed by isardSAT was deployed in the Montsec Astronomical Observatory (Lleida, Catalonia) in April 2021, about 4-km off-nadir of the nominal
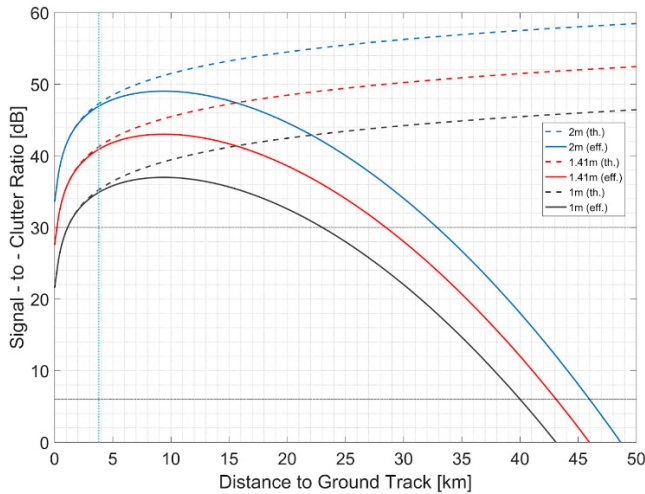
Fig. 1. Estimated SCR as a function of across-track distance to ground track for different sizes of square-side trihedral corner reflectors operating at Ku-band. A worse case backscattering clutter of 6 dB has been considered. For each size, two curves are plotted: the *theoretical* one without accounting for antenna beamwidth, and the *effective* one weighting the previous by twice the antenna beamwidth. The horizontal lines at 6 and 30 dB refer to the range and σ_0 requirements, while the vertical line marks the distance to ground track of the final selected location.

Sentinel-6A subsatellite track. Just after properly setting the satellite observation parameters over the area, maximum theoretical resolutions in both range and along-track dimensions were achieved in summer 2021, and since then, regular range measurements are taken roughly every ten days. The performance achieved is comparable to conventional active transponders in terms of range bias, datation bias, stability, and impulse response signal resolution. In this article, we provide the results from this first set of successful Sentinel-6A passes over the corner reflector.

This article is organized as follows: in Section II, we describe the design, manufacturing, and location of the corner reflector. The methodology and data processing are introduced in Section III, which is followed by the presentation of results in Section IV. Finally, the discussion and conclusions are addressed in Sections V and VI, respectively.

II. CORNER-REFLECTOR DESIGN AND LOCATION

A. Design

The theoretical radar cross section (RCS, σ) of a square-side trihedral corner reflector along its principal axis is [16]

$$\sigma = \frac{12\pi a^4}{\lambda^2} \tag{1}$$

where a is the side of a single plate and λ is the carrier frequency wavelength. On the other hand, the ratio between the RCS and the clutter is the so-called SCR

$$\mathrm{SCR} = \frac{\sigma}{\sigma_N A} \tag{2}$$

where the clutter is defined as the product of the clutter backscattering coefficient σ_N and the illuminated surface A, which for a radar altimeter is restricted to the cell represented by the along-track resolution and the across-track resolution projected to the ground (see Appendix for more details).

Since the effective ground resolution across-track gets smaller when moving away from the subsatellite track, a first

design conclusion is that, under the assumption of constant clutter density, the theoretical SCR increases when increasing the distance between the subsatellite track and the reflector. Nevertheless, off-nadir signals are in fact attenuated by the antenna pattern, resulting in an effective SCR as a function of distance from the ground track with a maximum at a certain off-nadir distance. This is depicted in Fig. 1 for Ku-band, where the differences between the theoretical SCR and the beamwidth-weighted SCR are shown for different corner sizes. The curves in the figure are estimated assuming background clutter independent of distance to ground track and nominal radar antenna beamwidth of 1.35°. A low clutter scenario with a backscattering coefficient of 6 dB has been considered. It can be observed that maximum effective SCR is found at off-track distances between 9 and 10 km, no matter the size of the corner as this particularity depends mainly on the antenna beamwidth. Note that the corner reflector antenna pattern has not been considered as it has a much wider beamwidth, close to 20° [14], and that the same integration time of 4.75 s is assumed for all ground track distances.

Minimum design SCR values of 6 and 30 dB for range and σ_0 calibration, respectively, were considered requirements as from [14]. The requirement for σ_0 calibration should be achieved at any reasonable distance to ground with corner-side dimensions higher than 1.6 m. Still, assuming that a certain off-nadir distance would be in practice unavoidable and that the final corner needed to be conveniently transported and installed, the final decision was to build a trihedral corner reflector made of three square plates of 1.414 m side length (2 m diagonal).

For a typical Ku-band radar altimeter, a corner reflector with this size yields a maximum RCS of 54.90 dBm^2, sufficient even under high clutter conditions only if the along-track resolution is properly reduced down to the meter scale with a FF-SAR algorithm. It must be noted that the choice of using squared plates instead of triangular plates provides an additional 9.5 dBm^2 in RCS with respect to the triangular shape. Under all these conditions, SCR higher than 30 dB should be achieved in locations at least about a few hundreds of meters from the ground track, which would enable not just range calibration but also σ_0 calibration.

B. Manufacturing

The reflector square plates, orthogonal to each other, are attached to the support structure, which consists of a triangular structure built with L-shaped bars. The nominal orientation of the reflector is zenith pointing, although there is 15° margin for optional off-zenith pointing. The whole apparatus is fastened with iron nails directly to the bedrock. Fig. 2 shows the corner reflector on its final placement.

The manufacturing and integration of the different parts must ensure that the global geometry of the system is kept, which includes plate planarity and inter-plate orthogonality. Indeed, for conventional radar altimeters operating at Ku-band, with a central frequency of 13.575 GHz for the Sentinel-6 Poseidon-4 case, the intra-plate planarity and inter-plate alignment require mechanical precision within 2 mm ($\sim \lambda/10$) in order to keep the reflector close to its theoretical RCS.

Fig. 2. Picture of the corner reflector at its final location at the Montsec Astronomical Observatory.

The following factors were therefore identified as potential distortions to the ideal orthogonality of the system.

1) Relative plate alignment.
2) Plate bending.
3) Thermoelastic distortion (TED).

The alignment between plates was considered the most critical aspect since it was dependent on the mechanical precision when positioning and drilling the screw holes over the whole structure. The potential plate bending due to gravity stress was addressed by means of a stress analysis, which pointed to a residual deflection of ∼1 mm at the top edges in case only the lower half of the plate was attached to the structure. Such deflection could be reduced to ∼0.1 mm by dedicated reinforcing. Finally, TED will occur if there is a variation in temperature over the structure. Except for fasteners, the structure consists of many separate pieces, which will have some thermal resistance at their interfaces. In the presence of strong sunlight, some parts will therefore become hotter than others. A dedicated analysis showed that an isolated panel normal to the maximum solar radiation could approach 200 °C. Although this does not consider radiation from the shadowed side, nor conduction to other parts of the structure nor convection, there is nevertheless the risk of some degree of TED with associated loss of orthogonality.

C. Location and Installation

The selection of the site was a compromise between: 1) proximity to subsatellite track for SCR optimization; 2) low background clutter; and 3) the presence of a safe and maintained emplacement.

The chosen location was the Montsec Astronomical Observatory Facility at 1564 m, on one of the summits of the Montsec ridge in the southern side of the Pyrenees. The prominence of the site was considered a key factor in order to minimize clutter and to avoid across-track ambiguities. In addition, the corner reflector could be placed a few tens of meters from the observatory dome and other buildings in the along-track direction, but still inside the facility area which ensures proper maintenance and protection.

The fact of being about 4 km off-nadir from the Sentinel-6A ground track ensures a proper illumination of the site, providing about 14 dB more than a hypothetical corner in nadir and with an antenna attenuation of less than 0.25 dB.

The overall area was considered clean enough in terms of environment as there are no trees nearby that could potentially accumulate leaves onto the corner and the animal presence is minimal. In terms of climate, the presence of snow in the area during winter is very reduced, so no further protecting radome was considered for a first measurement campaign.

The corner reflector was installed on April 16, 2021 at final coordinates 42.05190°N 0.73006°E. The corner vertex location was subsequently measured with a high-precision global navigation satellite system (GNSS) device in a dedicated geodetic campaign.

III. DATA PROCESSING AND METHODOLOGY

In this section, the global data processing chain is described.

A. From Raw Data to FF-SAR L1B

The European Space Agency (ESA) Sentinel-6 Poseidon-4 L1 Ground Processor Prototype [17], [18], developed by isardSAT, processes the L0 raw echoes up to L1A calibrated echoes. First, antenna gain, calibration parameters, and intra-burst corrections are applied in the L0 processor. Furthermore, window delay and datation are calculated when processing raw data to L1A product. After that, calibrated echoes in L1A files are processed with an in-house FF-SAR processor [19] in time domain based on the backprojection algorithm [15]. For each pass, all the echoes are aligned and phase-corrected before integration.

The focusing algorithm is applied on a set of along-track surfaces centered around the measured position of the vertex of the corner reflector, with the maximum available number of echoes for each pass. Zero padding is applied when waveforms are compressed in range with a factor of 8. The final result is a 2-D image in along-track and range dimensions. Since the corner reflector acts as a point-target, the expected shape of the 2-D image is a sinc-like function in both dimensions.

The choice of selecting a backprojection kernel in time domain rather than more computationally efficient options in frequency domain such as [20] lies in the fact that the former method is considered the most robust and precise method for high-accuracy applications, such as point target analysis.

The reference system of the full processing chain is ITRF2014, as this is the frame of the satellite orbital data as provided. However, the corner vertex location is exposed to the continental tectonic drift and its International Terrestrial Reference System (ITRS) coordinates are expected to change with time. To overcome this effect, the corner vertex coordinates, which were initially measured in ETRS89/00, need to be converted to equivalent ITRF2014 coordinates considering the specific epoch of each pass.

B. Determination of Range Bias, Datation Bias, and RCS

Three main outcomes are extracted from the FF-SAR radargram.

1) Range Bias: The measured uncorrected range is associated with the sample range of the waveform that presents higher intensity among the whole FF-SAR radargram. The range bias is the difference between the measured range and the expected slant range.

2) Datation Bias: The datation bias is the residual satellite time-stamping error of the transmitted pulses. It is obtained by determining the along-track bias of the waveform with higher intensity with respect to the corner location. Such a conversion is done by dividing the along-track bias by the ground velocity of the satellite. Alternative methods based on evaluating the phase slope [21] cannot be applied due to the high noise level in the phase function.

3) Radar Cross Section: The estimation of the RCS is based on the radar equation, which indicates the relationship between the power transmitted and received

$$\sigma = \frac{P_r}{P_t G^2 \lambda^2} (4\pi)^3 r^4 \qquad (3)$$

where

  P_r is the received power;
  P_t is the transmitted power;
  G is the antenna gain assumed equal for both transmitting and receiving;
  r is the distance between the corner reflector and the radar.

C. Geophysical Corrections

Range measurements are corrected for the following geophysical effects: wet and dry troposphere, vertical component of the solid Earth tide, ionospheric correction, ocean loading tide, and pole tide. Values for them are normally provided in L2 products [22] when operating in nominal SAR/RMC mode [9].

For the specific case of the dry and wet tropospheric delay corrections, two values are usually provided in the L2 files: values at sea-level altitude and values at satellite measurement altitude. The best performance has been found using the following approach: for the dry tropospheric correction, the model-based value at sea-level altitude has been projected to the actual corner reflector altitude assuming a linear model dependence [23], [24] and using local pressure and temperature measurements provided by the nearby Xarxa d'Estacions Meteorològiques Automàtiques (XEMA) weather station of the Catalan Meteorological Service. Regarding the wet tropospheric correction, the model-based value at measurement level has been considered being aware that, due to the unavailability of satellite radiometer measurements over land, the corrections provided are actually based on meteorological fields modeling [22].

In terms of datation geophysical corrections, it has been observed that the horizontal components of the solid Earth tide do affect the datation measurement. Indeed, the along-track position of the corner reflector due to this effect fluctuates in the order of ~0.1 m [25]. Data from [26] are used to estimate and correct for this effect.
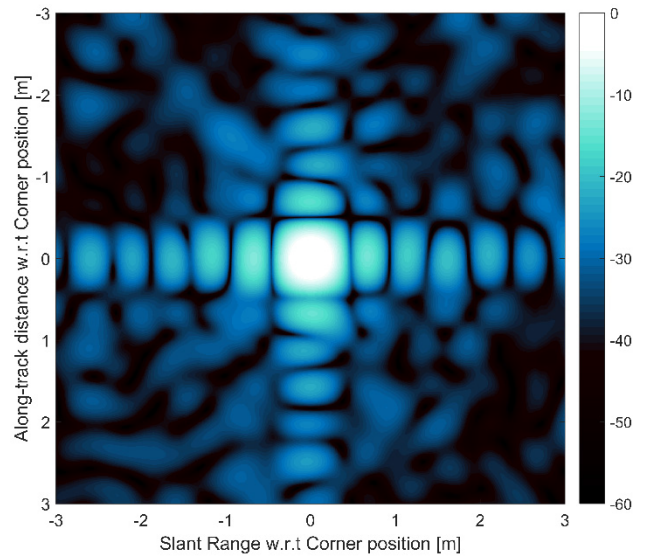

Fig. 3. Centered radargram with the 2-D impulse response function of the corner from the pass on October 25, 2021. The color scale represents normalized power in dB.

Finally, the received power is corrected by the attenuation from the atmosphere. Estimates of this correction are taken as well from L2 products.

IV. RESULTS

In this section, we present the results from a campaign of measurements obtained between September 25, 2021 and April 21, 2022, when the range window had already been adjusted to optimize the integration time. All passes within this period were successful except one that coincided with a snowstorm on November 23, 2021 and another one that was discarded because it coincided with a satellite maneuver on March 2, 2022.

For each pass, the satellite range window was operating at a requested fixed altitude along an 80-km path over the site. The acquisition power settings were adapted to properly amplify the expected power.

A. Impulse Response Functions and Resolutions

Fig. 3 shows the measured 2-D impulse response function of the corner reflector for the pass on October 25, 2021, processed with an integration time around 4.75 s and an along-track spacing of 0.01 m. For the sake of clarity, both dimensions in Fig. 3 have been interpolated with an additional factor of 16. According to the equations introduced in the Appendix, the theoretical along-track resolution is around 0.39 m, while the theoretical across-track resolution is 0.415 m. The measured along-track and across-track resolutions are estimated by assessing the amplitude of the main lobes to −3 dB along each dimension. This is better observed in Fig. 4, where the two impulse response functions are obtained by selecting the across-track and along-track waveforms that contain the maximum intensity in Fig. 3. Such approach yields an along-track and across-track resolutions of 0.43 and 0.415 m, respectively, consistent with expected values.

In terms of impulse function symmetry, the peak to sidelobe ratio (PSR) in across-track is 13 dB, while in along-track is
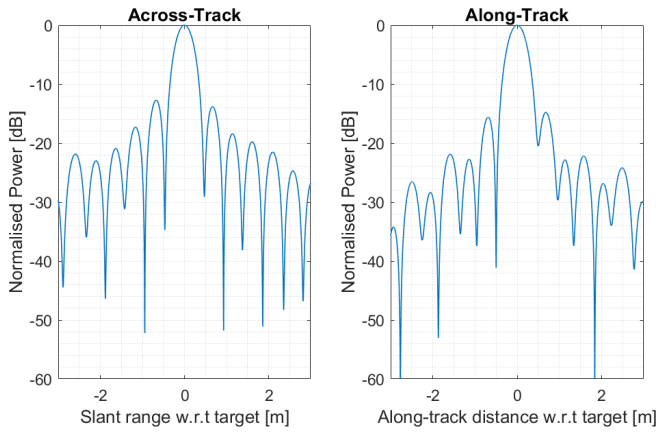
Fig. 4. (Left) Across-track impulse response function. (Right) Along-track impulse response function.
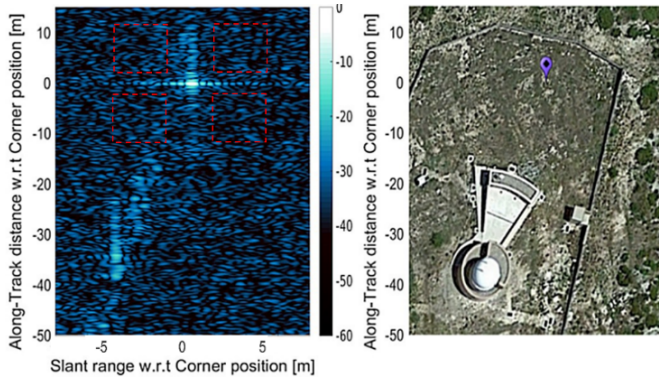

Fig. 5. (Left) Expanded radargram of the area to evaluate clutter incidence. (Right) Aerial image of the site aligned in the along-track direction. The corner imprint and some elements of the nearby Joan Oró telescope building are clearly appreciated. Colors refer to normalized power in dB. Clutter can be seen as blue speckles over the image. The red-dashed squares on the radargram represent the four quadrants with no signal used to estimate the clutter.
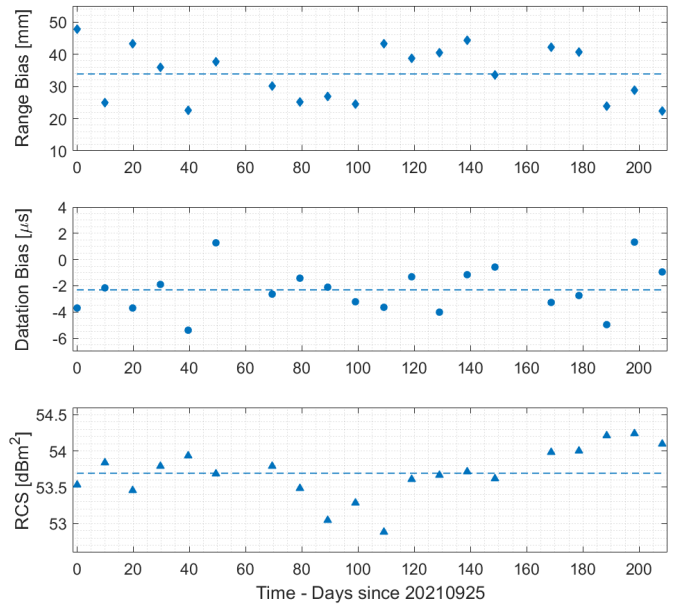

Fig. 6. (Top) Range bias for the full period after correcting for geophysical contributions and geometry. (Center) Datation bias for the same period corrected by solid Earth tide horizontal components. (Bottom) Measured RCS after compensating for the antenna pattern. All magnitudes are presented with dashed lines representing respective averaged values.

15 dB. For both cases, the difference between secondary lobes is within 1 dB.

The measured power and the range and datation bias are obtained from the along-track and across-track waveforms in Fig. 4 after applying an additional interpolation factor of 4, hence with an overall interpolation factor of 64 with respect to the output of the FF-SAR processor. Thus, while the power is determined from the maximum of the resulting waveforms, the range and datation bias are found in the offsets of the across-track and along-track functions, respectively.

B. Power, RCS, Background Clutter, and SCR

The measured power on the center of the lobes for this pass is -166.54 dBW, which by using (3) results in a measured RCS of 51.90 dBm^2 without compensating for the antenna pattern and 53.79 dBm^2 after compensating, differing the latter by 1.11 dBm^2 from the theoretical value.

In terms of environment clutter, as shown in Fig. 5, the echoes from the nearby buildings do not interfere with the reflector signal although they are clearly visible in the radar-gram. An average clutter of -207.15 dBW is obtained from the four quadrants without signal in Fig. 5, which yields an SCR of 40.61 dB, close to the performance estimated in Fig. 1.

C. Long-Term Series

The system stability is addressed by comparing a series of consecutive passes processed with comparable integration time (see Fig. 6). In terms of range, an average bias of 33.9 mm and a standard deviation of 8.5 mm are achieved after correcting for geophysical contributions. The datation bias measurements present a standard deviation of 5.04 μs (29.0 mm in along-track distance), which is reduced to 1.80 μs (10.3 mm) when corrected for horizontal components of the solid Earth tide. The mean datation after the correction is -2.31 μs (-13.3 mm).

The nonzero bias observed in both range and datation is consistent with the uncertainty of the corner vertex coordinates as measured during the GNSS campaign but may include as well residual systematic errors related with the application of the geophysical corrections, for instance, with the scaling to the measurement height for the wet and dry tropospheric corrections. No significant drifts can be appreciated over range and datation bias series, although it must be remarked that eventual plate motion and residual natural ground drift with respect to ETRS89 have been neglected since the same ETRS89 reflector vertex coordinates have been considered for the processing of all the passes.

Regarding the RCS, an average value of 53.69 dBm^2 with a standard deviation of 0.35 dBm^2 is found after compensating for the antenna pattern. The averaged difference with respect to the theoretical value is 1.2 dBm^2. This difference is consistent with the bias of 1.2–1.3 dB observed when comparing LR Ku σ_0 retrievals from Sentinel-6A with respect to Jason-3 as reported in the Sentinel-6 Michael Freilich Product Notice [27]. It must also be noted that the absolute σ_0 calibration by means of dedicated σ_0 transponders is still a pending activity at

the time of writing, which should take place in the upcoming months.

In terms of noise, residual noise in range and datation is preliminarily attributed to the overall uncertainty of the geophysical corrections, where the wet troposphere delay is likely to be the most prominent contributor for the range case due to its rapid spatial variation and consequent model complexity and uncertainty. Satellite orbit and attitude knowledge errors, instrument noise, and processing algorithms may also be contributing with minor incidence. Regarding the RCS, possible contributors are orbit drifts or thermoelastic effects. All three variables in Fig. 6 present a certain amount of low-frequency noise whose sources have not been identified yet but are likely to be attributed to the variability of some geophysical corrections or potentially other effects as described in [28]. In terms of possible correlation between variables, with the current dataset, no clear correlations are observed. Preliminary analysis suggests RCS correlation with closest distance to subsatellite track, which oscillates within passes. A detailed analysis of noise sources and correlation between measurables is left out of the scope of this article as more passes should be included.

V. DISCUSSION

Although passive corner reflectors are not expected to achieve the performance provided by active transponders, the success of this campaign confirms their utility in some radar altimeter key calibration aspects that need to be regularly monitored.

The site selection has been a key parameter for the success of the campaign. Undoubtedly, apart from the benefit of processing the data with a FF-SAR algorithm, the prominence of the site combined with its roughly 4-km distance to the subsatellite track keeps the clutter at very low levels. As already mentioned, in terms of SCR, the specific fact of being few kilometer off-track already provides around 14 dB extra with respect to a hypothetical identical reflector located at nadir.

It needs to be remarked that all the analysis presented has been done assuming only the ETRS89 drift with respect to the ITRS system, therefore neglecting eventual residual displacement due to local tectonic activity. A next step is thus to equip the facility with a permanent GNSS monitoring system able to track the local drift with high precision.

Regarding the overall final performance, it must be noted that there is still some margin of improvement mainly in the accuracy of the geophysical corrections, which could reduce even more the measured range and datation bias stability. Specifically, the uncertainty on the prediction of the wet troposphere delay is the limiting factor in range due to the unavailability of reliable radiometer measurements over the area. Indeed, complementing the site equipment with a local radiometer or with a dual frequency GNSS in order to provide a local measurement of the wet troposphere delay at the time of the radar altimeter passes, rather than using the estimates provided in the L2 files, would definitely allow to improve current performances.
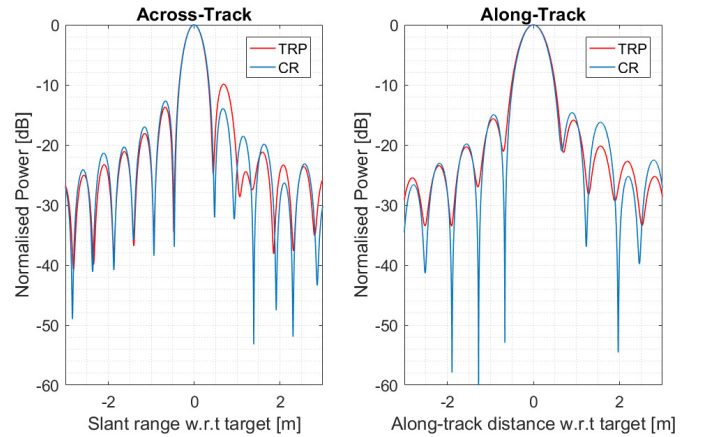

Fig. 7. Across-track and along-track impulse response functions for Sentinel-6A passes over the corner reflector and over the Crete transponder measured on March 22 and 29, 2022, respectively. The same integration time of 3.4 s is considered for both cases. Overall agreement is found in both facilities, except for some asymmetries in the secondary lobes.

Nevertheless, in comparison to what is currently achieved with active transponders, results from similar Sentinel-6A analysis with transponders [28], [29] report comparable bias and uncertainty for the range and the datation. Indeed, a range bias of -4 mm with an uncertainty of ± 9 mm is provided in [28], while typical values for range and datation of 6 ± 15 mm and -1 ± 6 μs, respectively, are provided in [29]. In terms of resolutions, similar values are obtained when processing the data with equivalent integration time. This is confirmed in Fig. 7, where the impulse response functions of a Sentinel-6A pass over the Crete transponder are compared with one over the corner reflector, both processed with an integration time of 3.4 s, the maximum available over the transponder. No major differences are observed in the main lobe, while minor asymmetries are visible only in the secondary lobes.

We have shown that, although being relatively simple structures, corner reflectors allow to measure radar altimeters' range, datation, and RCS on the same device, which is not commonly done when using active transponders.

Finally, as purely passive devices, corner reflectors are also attractive from the point of view of low cost, on-site operation, and maintenance. Ease and affordability of procurement and installation are likely to vary according to local circumstances.

VI. CONCLUSION

In this campaign, we have shown that trihedral corner reflectors are capable of providing key external calibration measurements for periodic radar altimeter performance monitoring. Data from regular Sentinel-6A passes over the reflector have been processed with a FF-SAR algorithm implemented in the time domain. Results from this campaign may have an impact on calibration strategies for current and future radar altimeters, such as CryoSat-2, Sentinel-3, Sentinel-6, and CRISTAL.

APPENDIX

The expressions used to determine the radar altimeter theoretical resolutions in along-track, across-track, and ground projected are introduced in this Appendix.

The along-track resolution is inversely proportional to the integration time, achieving the maximum along-track resolution when the whole target illumination time, determined by the antenna beam pattern, is processed. Therefore, the system theoretical along-track resolution, given in meters, is defined as [15], [30]

$$\Delta_{\mathrm{al}} = 0.886 \frac{\lambda H_{\mathrm{sat}}}{2 V_{\mathrm{sat}} T_{\mathrm{int}}} \qquad (4)$$

where H_{sat} and V_{sat} are the satellite altitude and nominal velocity, respectively, λ is the carrier frequency length, and T_{int} is the integration time. The factor 0.886 accounts for the half-power beamwidth criteria.

In the across-track direction, the range resolution after matched filtering only depends on the pulse chirp bandwidth B and is determined, in slant range units, by the following equation [15], [30]:

$$\Delta_{\mathrm{ac}} = 0.886 \frac{c}{2B} \qquad (5)$$

where c is the speed of light and the factor 0.886 accounts again for the half-power beamwidth criteria.

Finally, for a given slant range spacing, the range sample spacing projected to the ground (Δ_g) varies with the local incidence angle θ_i, which refers to the angle between the incident radar pulse and the vector perpendicular to the ground surface [30]:

$$\Delta_g = \frac{\Delta_{ac}}{\sin \theta_i} \qquad (6)$$

ACKNOWLEDGMENT

REFERENCES

[1] S. Abdalla et al., "Altimetry for the future: Building on 25 years of progress," *Adv. Space Res.*, vol. 68, pp. 319–363, Mar. 2021, doi: 10.1016/j.asr.2021.01.022.

[2] H. Eldardiry, F. Hossain, M. Srinivasan, and V. Tsontos, "Success stories of satellite radar altimeter applications," *Bull. Amer. Meteorolog. Soc.*, vol. 103, no. 1, pp. 33–53, Jan. 2022, doi: 10.1175/BAMS-D-21-0065.1.

[3] A. Cazenave et al., "Observational requirements for long-term monitoring of the global mean sea level and its components over the altimetry era," *Frontiers Mar. Sci.*, vol. 6, p. 582, Sep. 2019, doi: 10.3389/fmars.2019.00582.

[4] B. Haines, S. D. Desai, D. Kubitschek, and R. R. Leben, "A brief history of the harvest experiment: 1989–2019," *Adv. Space Res.*, vol. 68, no. 2, pp. 1161–1170, Jul. 2021, doi: 10.1016/j.asr.2020.08.013.

[5] R. J. Powell, "Relative vertical positioning using ground-level transponders with the ERS-1 altimeter," *IEEE Trans. Geosci. Remote Sens.*, vol. GE-24, no. 3, pp. 421–425, May 1986, doi: 10.1109/TGRS.1986.289601.

[6] N. Pierdicca et al., "Transponder calibration of the ENVISAT RA-2 altimeter Ku band sigma naught," *Adv. Space Res.*, vol. 51, no. 8, pp. 1478–1491, Apr. 2013, doi: 10.1016/j.asr.2012.12.014.

[7] D. J. Wingham et al., "CryoSat: A mission to determine the fluctuations in earth's land and marine ice fields," *Adv. Space Res.*, vol. 37, no. 4, pp. 841–871, 2006.

[8] C. Donlon et al., "The global monitoring for environment and security (GMES) Sentinel-3 mission," *Remote Sens. Environ.*, vol. 120, pp. 37–57, May 2012, doi: 10.1016/j.rse.2011.07.024.

[9] C. J. Donlon et al., "The Copernicus Sentinel-6 mission: Enhanced continuity of satellite sea level measurements from space," *Remote Sens. Environ.*, vol. 258, Jun. 2021, Art. no. 112395, doi: 10.1016/j.rse.2021.112395.

[10] A. Garcia-Mondéjar, M. Fornari, J. Bouffard, P. Féménias, and M. Roca, "CryoSat-2 range, datation and interferometer calibration with svalbard transponder," *Adv. Space Res.*, vol. 62, no. 6, pp. 1589–1609, Sep. 2018, doi: 10.1016/j.asr.2018.01.008.

[11] S. Mertikas et al., "The ESA permanent facility for altimetry calibration: Monitoring performance of radar altimeters for Sentinel-3A, Sentinel-3B and Jason-3 using transponder and sea-surface calibrations with FRM standards," *Remote Sens.*, vol. 12, no. 16, p. 2642, Aug. 2020, doi: 10.3390/rs12162642.

[12] A. W. Doerry, "Reflectors for SAR performance testing," Sandia Nat. Lab. (SNL-NM), Albuquerque, NM, USA, Tech. Rep., SAND2014-0882, 2014, doi: 10.2172/1204079.

[13] R. K. Raney, "The delay/Doppler radar altimeter," *IEEE Trans. Geosci. Remote Sens.*, vol. 36, no. 5, pp. 1578–1588, Sep. 1998, doi: 10.1109/36.718861.

[14] C. R. Francis, "Sentinel requirements assessment: Corner reflector definition, installation and location," GerSpatial, La Romieu, France, Tech. Rep., PR-GER-TN-007, Jan. 2020.

[15] A. Egido and W. Smith, "Fully focused SAR altimetry: Theory and applications," *IEEE Trans. Geosci. Remote Sens.*, vol. 55, no. 1, pp. 392–406, Jan. 2017, doi: 10.1109/TGRS.2016.2607122.

[16] E. F. Knott, J. F. Shaeffer, and M. T. Tuley, *Radar Cross Section*. Norwood, MA, USA: Artech House, 1993.

[17] E. Makhoul et al., "The Sentinel-6 Poseidon-4 ground processor prototype: New simulation results," in *Proc. Ocean Surf. Topography Sci. Team (OSTST) Meeting*, Oct. 2017.

[18] C. Donlon, R. Cullen, L. Giulicchi, M. Fornari, and P. Vuilleumier, "Copernicus Sentinel-6 Michael freilich satellite mission: Overview and preliminary in orbit results," in *Proc. IEEE Int. Geosci. Remote Sens. Symp. IGARSS*, Jul. 2021, pp. 7732–7735, doi: 10.1109/IGARSS47720.2021.9553731.

[19] F. Gibert et al., "Results of the dragon 4 project on new ocean remote sensing data for operational applications," *Remote Sens.*, vol. 13, no. 14, p. 2847, Jul. 2021, doi: 10.3390/rs13142847.

[20] P. Guccione, M. Scagliola, and D. Giudici, "2D frequency domain fully focused SAR processing for high PRF radar altimeters," *Remote Sens.*, vol. 10, no. 12, p. 1943, Dec. 2018, doi: 10.3390/rs10121943.

[21] M. Scagliola and P. Guccione, "Datation and range calibration of radar altimeter exploiting fully focused SAR processing," *IEEE Geosci. Remote Sens. Lett.*, vol. 18, no. 3, pp. 480–483, Mar. 2021, doi: 10.1109/LGRS.2020.2980635.

[22] *SENTINEL-3 Products and Algorithms Definition (S3PAD)*, CLS, document CLS-DOS-NT-09-119, S3PAD-RS-CLS-SD03-00017, 2011.

[23] M. Fernandes, C. Lázaro, A. Nunes, and R. Scharroo, "Atmospheric corrections for altimetry studies over inland water," *Remote Sens.*, vol. 6, no. 6, pp. 4952–4997, May 2014, doi: 10.3390/rs6064952.

[24] J. P. Collins, "Assessment and development of a tropospheric delay model for aircraft users of the global positioning system," M.S. thesis, Dept. Geodesy Geomatics Eng., Univ. New Brunswick, Fredericton, NB, Canada, 174, 1999.

[25] S. K. Poulsen, "Tidal deformation of the solid earth: A finite difference discretization," M.S. thesis, Niels Bohr Inst., Copenhagen, Denmark, 2009, Accessed: May 2022. [Online]. Available: https://web.archive.org/web/20161011123826/http://cct.gfy.ku.dk/thesis/thesis_stinekp.pdf

[26] D. Milbert. *Solid Earth Tide*. Accessed: May 2022. [Online]. Available: http://geodesyworld.github.io/SOFTS/solid.htm

[27] *Copernicus Sentinel-6 Michael Freilich Product Notice (Altimetry)*, EUMETSAT document EUM/RSP/DOC/21/1230254, Nov. 2021.

[28] S. P. Mertikas et al., "Performance evaluation of the CDN1 altimetry Cal/Val transponder to internal and external constituents of uncertainty," *Adv. Space Res.*, vol. 70, no. 8, pp. 2458–2479, Oct. 2022, doi: 10.1016/j.asr.2022.07.001.

[29] S. Amraoui et al., "New results of Sentinel-6 transponder working group," *Presentation at the 3rd Sentinel-6 Validation Team Meeting*, Oct. 2021, Accessed: Jul. 2022. [Online]. Available: https://www.eventsforce.net/eumetsat/frontend/reg/thome.csp?pageID=12320&ef_sel_menu=202&eventID=29

[30] I. G. Cumming and F. H. Wong, "Digital processing of synthetic aperture radar data: Algorithms and implementation,' *Artech House*, vol. 1, no. 3, pp. 108–110, 2005.

Ferran Gibert received the M.S. degree in aerospace engineering and the Ph.D. degree in aerospace science and technology from the Universitat Politècnica de Catalunya, Barcelona, Spain, in 2011 and 2016, respectively. His Ph.D. was focused on the design of thermal diagnostics experiments for the LISA Pathfinder mission.

From 2016 to 2018, he completed a post-doctoral research with the University of Trento, Trento, Italy, from where he supported the LISA Pathfinder operations and data analysis phase. Since June 2018, he has been a Research and Development Engineer with isardSAT, Barcelona, being currently involved in the development of algorithms for radar altimeter processors.

Adrià Gómez-Olivé received the bachelor's degree in telecommunications technologies and services engineering from the Universitat Politècnica de Catalunya, Barcelona, Spain, in 2022, where he is currently pursuing the M.S. degree in advanced telecommunication technologies.

He joined isardSAT, Barcelona, in 2021. His tasks include the implementation and handling of processing techniques of SAR altimetry data for calibration and monitoring tools and the analysis of inland water level and extension from altimetry data measurements.

Albert Garcia-Mondéjar received the M.S. degree in telecommunications engineering from the Universitat Politècnica de Catalunya, Barcelona, Spain, in 2009.

He joined isardSAT, Barcelona, Spain, in 2011, where he is currently a Senior Altimetry Engineer and the Research and Development Manager. He has wide experience in algorithm development, from $L0$ to $L2$, for SAR altimetry missions. His fields of expertise include the improvement of $L1$ algorithms, instrument calibration, science multimission activities, and innovative methods to improve performances over complex scenarios.

Richard Francis received the B.Sc. degree in physics and the Ph.D. degree in space physics from the University of Sheffield, Sheffield, England, in 1974 and 1979, respectively.

He worked six years in industry on spacecraft feasibility studies and algorithm development for Nimbus 7's SMMR and SeaSat's altimeter. In 1983, he took a post in the ERS-1 Team at ESA/ESTEC Noordwijk, The Netherlands. He spent more than 30 years at ESA working on a variety of missions, all except one of which carried a radar altimeter. He progressed from an Altimeter System Engineer through a Mission and System Engineer and finally the Project Manager for his last two missions. After retirement in 2015, he has continued to participate in the development of ESA's missions.

Sergi Hernández received the M.S. degree in telecommunications engineering from the Universitat Politècnica de Catalunya, Barcelona, Spain, in 2020. He is currently pursuing the Ph.D. degree in signal theory and communications with the Universitat Politècnica de Catalunya, Barcelona, Spain, in collaboration with isardSAT, Barcelona.

In 2019, he joined isardSAT as an Research and Development Engineer. His main activities are the research, development, and implementation of altimetry data processing algorithms.

Adrián Flores de la Cruz received the M.S. and Ph.D. degrees in telecommunications engineering from the Polytechnic University of Cartagena, Murcia, Spain, in 2014 and 2019, respectively.

From 2017 to 2019, he was with Hisdesat SA, Madrid, Spain, as a Cal/Val Engineer, where he worked on the PAZ Mission. Since March 2019, he has been a Research and Development Engineer with isardSAT, Barcelona, Spain, working on the development and implementation of data processing techniques with special focus on the instrumental calibration.

Ester Vendrell is currently the Operations Manager with isardSAT, Barcelona, Spain, and has more than 15 years of experience in managing research and operational projects in Earth observation, including corner reflector deployment projects for InSAR applications.

Mònica Roca i Aparici received the M.S. degree in electronics and telecommunication engineering from the Universitat Politècnica de Catalunya, Barcelona, Spain, in 1995.

She has been the Director of isardSAT, Barcelona, Spain, since 2006. She has been actively involved in the design and development of on-board and on-ground algorithms (including instrument calibration and up to Level-2 retacking algorithms) to process data mainly from radar altimetry instruments on-board ESA satellites and in all satellite mission phases, for more than 20 years.